

Direct Observation of Dirac Cones and a Flatband in a Honeycomb Lattice for Polaritons

T. Jacqmin,¹ I. Carusotto,² I. Sagnes,¹ M. Abbarchi,^{1,*} D. D. Solnyshkov,³ G. Malpuech,³ E. Galopin,¹
A. Lemaître,¹ J. Bloch,¹ and A. Amo¹

¹*Laboratoire de Photonique et Nanostructures, CNRS/LPN, Route de Nozay, 91460 Marcoussis, France*

²*INO-CNR BEC Center and Dipartimento di Fisica, Università di Trento, I-38123 Povo, Italy*

³*Institut Pascal, PHOTON-N2, Clermont Université, Université Blaise Pascal,*

CNRS, 24 avenue des Landais, 63177 Aubière Cedex, France

(Received 30 October 2013; published 18 March 2014)

Two-dimensional lattices of coupled micropillars etched in a planar semiconductor microcavity offer a workbench to engineer the band structure of polaritons. We report experimental studies of honeycomb lattices where the polariton low-energy dispersion is analogous to that of electrons in graphene. Using energy-resolved photoluminescence, we directly observe Dirac cones, around which the dynamics of polaritons is described by the Dirac equation for massless particles. At higher energies, we observe p orbital bands, one of them with the nondispersive character of a flatband. The realization of this structure which holds massless, massive, and infinitely massive particles opens the route towards studies of the interplay of dispersion, interactions, and frustration in a novel and controlled environment.

DOI: 10.1103/PhysRevLett.112.116402

PACS numbers: 71.36.+c, 42.65.Tg, 73.22.Pr, 78.67.-n

Engineering Hamiltonians in controlled systems has proven to be a useful tool to simulate and unveil complex condensed matter phenomena otherwise experimentally inaccessible. Indeed, condensed-matter systems usually lack control and observables, whereas model systems such as ultracold atoms [1], arrays of photonic waveguides [2], or polariton gases [3] enable the control of the density, the temperature, and, in the case of lattice systems, the topology of the band structure. In this context, the honeycomb lattice, whose geometry is responsible for the properties of graphene, has attracted a lot of attention. This extraordinary material shows pointlike intersections between the conduction and valence bands. Around those points, referred to as Dirac points, the energy dispersion is linear, and electrons behave like massless relativistic particles [4]. The honeycomb geometry gives rise to intriguing phenomena such as anomalous Klein tunneling and geometric phase effects that result in the antilocalization of electrons [4]. In addition, geometric frustration in the honeycomb lattice is expected to give rise to nondispersive bands in which all states are localized [5]. These bands have not yet been experimentally evidenced.

The investigation of this physics has triggered the realization of simulators [6] whose parameters can be controlled in a range not easily accessible in graphene. For instance, honeycomb lattices for cold atoms [7,8], electrons in solids [9] and molecules [10], and acoustic waves [11] were realized. In photonics, honeycomb lattices were created using light-induced lattices in nonlinear crystals [12], microwave-domain photonic crystals [13], arrays of coupled waveguides [14,15], and resonators [16]. While these systems have shown remarkable features like topological phase transitions [8] or the possibility of

including synthetic gauge fields [14], they lack simultaneous control of the particle momentum, local potential, interactions and on-site visualization. In this sense, polaritons in semiconductor planar microcavities appear as an extraordinary platform overcoming these limitations [3]. These light-matter particles, which arise from the strong coupling between cavity photons and quantum well excitons can be created, manipulated and detected using optical techniques. Two-dimensional lattices for polaritons have been implemented using surface acoustic waves [17] and gold deposition at the surface of the cavity [18–20]. However, the former method allows very limited lattice geometries, while the latter can only provide very shallow modulations of the potential. Alternatively, the recent realization of coupled micropillars based on deep etching of a planar structure [21,22] has opened the way towards the engineering of lattices for polaritons with controlled tunneling and deep on-site potentials with arbitrary geometry.

In this Letter, we report on a honeycomb lattice for polaritons, made of hundreds of coupled micropillars etched in a planar semiconductor microcavity. By monitoring the photoluminescence at low excitation density, we directly image the energy dispersion of the structure, which reveals several energy bands. The lowest two arise from the coupling between the fundamental modes of the micropillars. They are analogous to the π and π^* bands of graphene [4]. In particular, we evidence six Dirac cones at the corners of the first Brillouin zone (Bz), around which the energy dispersion is linear. When increasing the excitation intensity, we observe polariton condensation occurring at the top of the π^* band, showing spatial coherence extended over the whole excitation spot. Additionally, we

report on the presence of higher-energy bands arising from the coupling between higher-energy modes of the pillars. In particular, we observe a nondispersive band in which polaritons have an infinite effective mass. The observation of this flatband opens the way to the study of the interplay of interactions, frustration, and spin dynamics in a novel driven-dissipative framework.

Our structure is a $Q = 72000 \lambda/2$ microcavity. It is a $\text{Ga}_{0.05}\text{Al}_{0.95}\text{As}$ layer surrounded by two $\text{Ga}_{0.05}\text{Al}_{0.95}\text{As}/\text{Ga}_{0.8}\text{Al}_{0.2}\text{As}$ Bragg mirrors with 28 (40) top (bottom) pairs. Twelve GaAs quantum wells of 7 nm width are inserted inside the cavity, yielding a 15 meV Rabi splitting. Experiments are performed at 10 K and -17 meV cavity-exciton detuning. We engineer a honeycomb lattice of coupled micropillars by using electron beam lithography and dry etching of the sample down to the GaAs substrate [see Fig. 1(a)]. The diameter of each pillar is $d = 3 \mu\text{m}$, and the distance between two adjacent pillars (the lattice constant), is $a = 2.4 \mu\text{m}$. The etched cavity shows a polariton lifetime of 27 ps at the bottom of the lower polariton band. As the interpillar distance is smaller than their diameter, the pillars spatially overlap [see Fig. 1(b)]. This results in a sizable polariton tunnel coupling between adjacent micropillars via their photonic component [22]. For our structure, the tunnel coupling amounts to 0.25 meV. The system is excited out of resonance with a Ti:Sapph monomode laser at 730 nm, in a spot of $30 \mu\text{m}$ diameter covering around 30 pillars. The photoluminescence is collected through a high numerical aperture objective

(NA = 0.65), dispersed in a spectrometer and detected by a CCD camera on which we can image either the real or the momentum space. Note that a chopper was used in the case of high power excitation to avoid heating of the sample.

Under low-power excitation, incoherent relaxation of polaritons results in the population of all the energy bands. Note that for low power excitation polariton-polariton interactions are negligible so that single particle physics of the honeycomb lattice is probed. Figure 1(d) shows the measured far field photoluminescence containing many groups of bands, separated by energy gaps. The two lowest bands (*S* bands) arise from the coupling between the fundamental mode of the pillars (*S* modes). At higher energy, we observe a group of four bands (*P* bands) arising from the coupling between the first excited state of the pillars, which is twice degenerate and has two lobes [22] [see Fig. 1(e)]. The separation between these two groups of bands is $\Delta E = 3.2 \text{ meV}$, the energy difference between the two lowest-energy states of the individual pillars. Above those two lowest-energy states of the individual pillars, many others can be seen arising from the hybridization of higher energy modes of the pillars.

The two *S* bands stem from the coupling between micropillar states which have a cylindrical symmetry similar to that of the carbon P_z electronic orbitals in graphene. Thus, we expect the two *S* bands to present features analogous to the π and π^* bands of graphene, including six Dirac (contact) points [4] in the first Bz [see Fig. 1(c)]. Figure 2(a) shows the measured emitted intensity in momentum space at the Dirac points energy [zero energy in Fig. 1(d)]. We observe the six Dirac points at the corner of the first Bz (yellow points). The adjacent Bzs are also seen. Figures 2(b) and 2(c) show the measured energy resolved emission along the lines 1 and 2 indicated in Fig. 2(a), passing through four and three Dirac linear intersections respectively. As the confinement energy on each site of the lattice is much larger than the tunneling energy, the system is well described by the tight-binding approximation. Including first- and second-neighbor tunneling, the following dispersion can be obtained [4],

$$E(\mathbf{k}) = \pm t \sqrt{3 + f(\mathbf{k})} - t' f(\mathbf{k}), \quad (1)$$

where

$$f(\mathbf{k}) = 2 \cos(\sqrt{3}k_y a) + 4 \cos\left(\frac{\sqrt{3}}{2}k_y a\right) \cos\left(\frac{3}{2}k_x a\right). \quad (2)$$

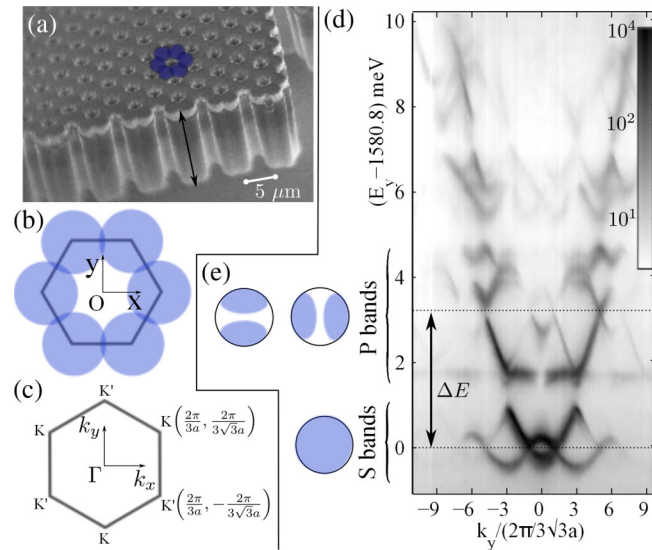


FIG. 1 (color online). (a) Scanning electron microscope image of a corner of the microstructure. One hexagon of pillars is underlined with blue disks. The dark arrows show the growth axis of the cavity. The overlap between pillars is sketched in (b). (c) First Bz. (d) Measured momentum space energy resolved photoluminescence at $k_x = -2\pi/3a$ [line 0 in Fig. 2(a)], under nonresonant low-power excitation. (e) Sketch of the real space distribution of *S* and *P* modes in a single pillar.

By fitting Eq. (1) to the data in Fig. 2 we extract a value of the coupling between first and second neighbors of $t = 0.25$ and $t' = -0.02 \text{ meV}$, respectively. The result of the fit is shown in Fig. 2(b), and yields a group velocity $v = 3at/2\hbar = 1.3 \times 10^6 \text{ m.s}^{-1}$ around the Dirac points. Note that the data shown in Fig. 2(b) do not belong to the first Bz. If we perform the same measurement along line 3 in

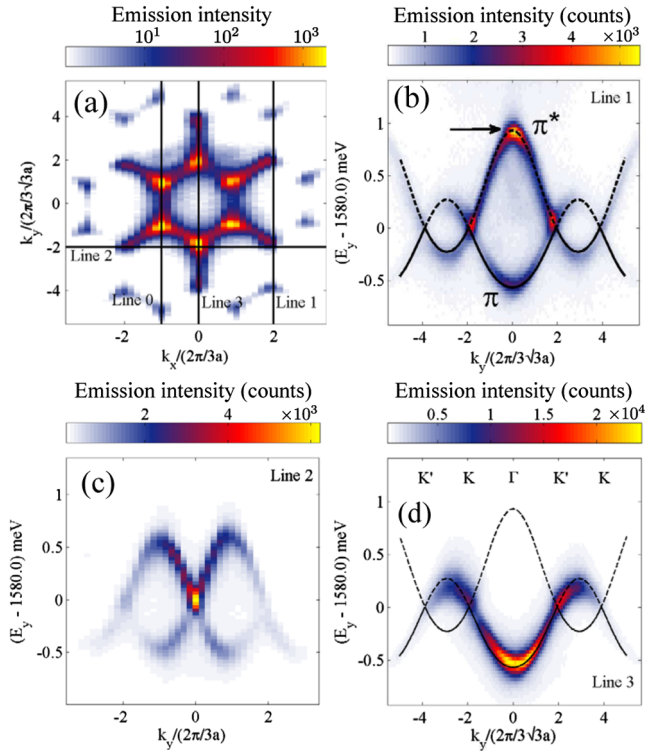


FIG. 2 (color online). (a) Measured photoluminescence intensity in momentum space at the energy of the Dirac points [dotted line in Fig. 1(d)]. (b) Spectrally resolved far field emission along line 1 in (a). The black line is a fit to Eq. (1). (c) Same as (b) along line 2 in (a). (d) Spectrally resolved far field emission along line 3 in (a), passing through the first Bz.

Fig. 2(a), we show in Fig. 2(d) that the emission is absent in the upper band (dashed line) within the first Bz, and in the lower band (solid line) within the second Bz. This phenomenon arises from destructive interference in the far field emission along certain high symmetry directions. It occurs in lattices with multiple sites per unit cell [23] and has been observed along the K - Γ - K' directions in angle-resolved electron spectroscopy measurements in graphene [24].

By increasing the excitation intensity, we observe polariton condensation, as evidenced by the threshold in the integrated emission intensity [Fig. 3(d)]. The threshold power is similar to that observed in a planar structure [25]. The low value of the measured emission blueshift, due to interactions between polaritons and uncondensed excitons, [see Fig. 3(d)] certifies that the system remains in the strong coupling regime across the threshold [26]. Moreover, the emission spectrum collapses into a single emission line, and extended spatial coherence builds up. By monitoring the energy-resolved emitted intensity across the condensation threshold, we observe that condensation takes place at the top of the π^* band [arrow in Fig. 2(b), [27]]. This state is located at the Γ point (center of the Bzs) as seen in Fig. 3(a). The far field destructive interference discussed above results in the absence of emission from the center of the first Bz, marked by a cross in Fig. 3(a).

The real space emission of the condensate is shown in Fig. 3(b), covering the same area as the pump spot. The intensity maxima are centered on the pillars as expected for a state arising from the hybridization of S states. We extract its phase structure as follows: we magnify the image of one pillar, and make it interfere with an image of the whole excited region [28]. The normalized interference pattern, without energy selection, is shown in Fig. 3(c) above the condensation threshold. We observe spontaneous coherence over the whole size of the pump beam. At the intersection between two adjacent pillars [white square in Fig. 3(c)], the fringes are shifted by half a period. Thus there is a π phase shift between adjacent pillars, as expected for the antibonding π^* band. Note that condensation does not take place in the ground state. This feature arises from the out of equilibrium nature of polaritons in which the steady state is fixed by the interplay between pump, relaxation and decay [29,30]. The antibonding mode at the Γ point favors condensation due to two features: (i) its negative effective mass and positive interaction energy and (ii) its longer lifetime, which stems from the antisymmetric character of the state [31] and from the lower nonradiative recombination rate due to the vanishing polariton density at the constrictions between pillars, where the defect density is larger.

We have shown that the two S bands mimic the graphene π and π^* bands. But the honeycomb lattice contains more

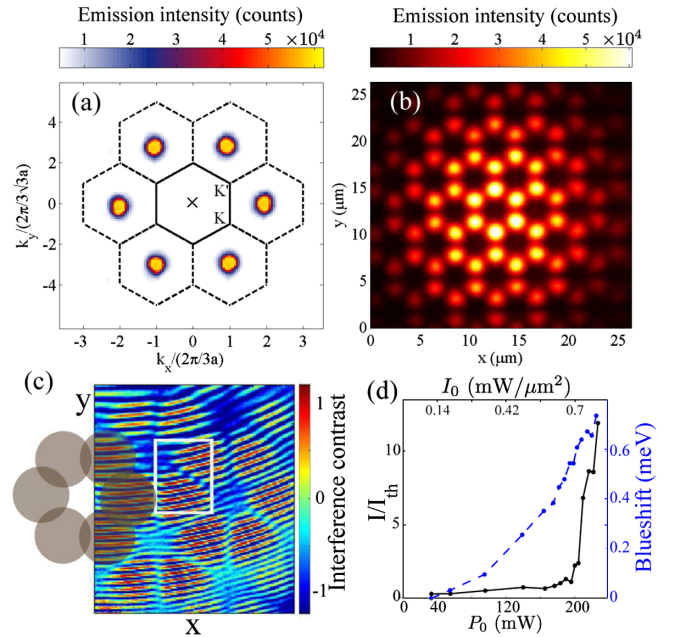


FIG. 3 (color online). (a) Photoluminescence emission in momentum space above the condensation threshold. The black solid/dashed line shows the first/second Bz. (b) Real space image of the condensed state. (c) Interference pattern above condensation threshold. The position of six pillars is underlined with gray disks. (d) Total emitted intensity (black line) and blueshift of the polariton emission at the top of the π^* band (blue dashed line) as a function of excitation intensity I_0 or power P_0 .

than those bands if higher orbital modes are available. In our lattice, the coupling between P modes of the pillars leads to four energy bands which appear above the two S bands, separated by a gap of about 0.7 meV [see Fig. 1(d)]. The P bands are shown in detail in Fig. 4(a) revealing that the lowest one is flat. Flatbands are characterized by an infinite effective mass and, consequently, a vanishing kinetic energy. In this situation, one can show that all states are localized without interaction [32]. Moreover, weak interactions have been predicted to give rise to strongly correlated phases in a lossless system [5,33]. To understand the origin of the flatbands, one can extend the usual tight-binding treatment to P states with a Hamiltonian of the form [5,34]

$$\hat{H} = -\sum_{\langle i,j \rangle} [t_{\parallel} (\hat{\psi}_i^{\dagger} \cdot e_{ij}^{(L)}) (e_{ij}^{(L)\dagger} \cdot \hat{\psi}_j) + t_{\perp} (\hat{\psi}_i^{\dagger} \cdot e_{ij}^{(T)}) (e_{ij}^{(T)\dagger} \cdot \hat{\psi}_j) + \text{H.c.}] \quad (3)$$

For each ij link, the $e_{ij}^{(L,T)}$ unit vectors are directed respectively along and orthogonally to the link direction. In the Hamiltonian, they serve to extract the projections of the P state respectively along and orthogonal to the link. The t_{\parallel} amplitude then describes hopping between P states with main lobes located along the link, while t_{\perp} describes

the (typically much weaker) hopping between states with lobes located sideways to the link. In the limiting case where $t_{\perp} = 0$ meV and $t_{\parallel} = -1$ meV, the eigenstates of Eq. (3) give rise to four energy bands plotted in Fig. 4(c). The two extreme bands are flat, the two intermediate ones are dispersive. For those parameters, this model describes well the lower bands observed in the experiment [Fig. 4(a)]. However, the higher energy band in Fig. 4(a) is not flat. This can be explained by allowing for a weak hopping also for the P states orthogonal to the link. Indeed in the case where $t_{\perp} = 0.2$ and $t_{\parallel} = -1$ meV, the tight-binding result is plotted in Fig. 4(d), where the two extreme bands are no longer flat. The band structure reported in Fig. 4(a) can then be understood assuming that t_{\perp} increases with the energy, resulting in a flatband ($t_{\perp} \approx 0$) at low energy and a dispersive band ($t_{\perp} \approx 0.2$ meV) at higher energy. Indeed, the tunneling probability varies exponentially with the barrier height relative to the state, and thus increases strongly for higher energy states. In order to confirm this model, we have performed a numerical simulation of the two-dimensional Schrödinger equation which reproduces the observed dispersion [27]. Finally, Fig. 4(b) shows the flatband real space mode for which intensity maxima sit between the pillars, thus arranged in a kagome geometry.

In summary, we have implemented a system which allows direct optical access to the basic properties of engineered lattices as demonstrated by the direct observation of Dirac cones in a honeycomb geometry. The position, shape and size of each lattice site can be controlled at will during fabrication. Moreover, via resonant excitation of the structure, polariton wave packets can be created with any desired energy and momentum. This configuration has been previously used to evidence polariton flow without scattering and the hydrodynamic nucleation of vortices and solitons [3]. It opens the way to study a number of effects in the honeycomb lattice, like Klein tunneling at a potential step [35], the geometrical Berry curvature of the bands [36] and the topological physics in the presence of synthetic gauge fields [14]. The observation of a bright flatband suggests the possibility of using a resonant pump to selectively inject polaritons into it and investigate the interplay between frustration, dispersion, and interactions in such flatbands [5,33].

This work was supported by the French RENATECH, the ANR-11-BS10-001 contract “QUANDYDE,” the RTRA Triangle de la Physique (Contract “Boseflow1D”), the FP7 ITNs “Clermont4” (235114), the FP7 IRSES “Polaphen” (246912), the POLATOM ESF Network, the Labex Nanosaclay, and the ERC (Honeypol and QGBE).

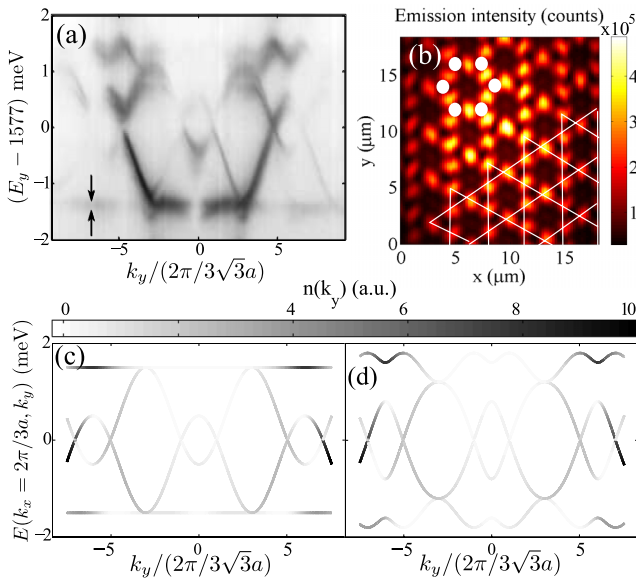


FIG. 4 (color online). (a) Zoom on the four P bands shown in Fig. 1(d). (b) Real space image integrated in energy over the flatband, marked with two arrows in (a). The centers of six pillars are shown in white disks. The kagome geometry of the emission lobes is underlined with white lines. (c) and (d): calculated energy dispersion at $k_x = -2\pi/3a$ [same direction as in (a)] from Eq. (3) for $t_{\parallel} = -1$, $t_{\perp} = 0$, and (c) $t_{\perp} = 0.2$ meV (d). For each state, the color scale indicates the relative brightness of its emission at energy E and wave vector k_y , as predicted by the Fourier transform of the spatial wave function.

*Present address: IM2NP, Aix-Marseille Université, UMR CNRS 6242, 13997 Marseille, France.

- [1] I. Bloch and W. Zwerger, *Rev. Mod. Phys.* **80**, 885 (2008).
- [2] A. Szameit and S. Nolte, *J. Phys. B* **43**, 163001 (2010).
- [3] I. Carusotto and C. Ciuti, *Rev. Mod. Phys.* **85**, 299 (2013).

- [4] A. H. Castro Neto, N. M. R. Peres, K. S. Novoselov, and A. K. Geim, *Rev. Mod. Phys.* **81**, 109 (2009).
- [5] C. Wu, D. Bergman, L. Balents, and S. Das Sarma, *Phys. Rev. Lett.* **99**, 070401 (2007).
- [6] M. Polini, F. Guinea, M. Lewenstein, H. C. Manoharan, and V. Pellegrini, *Nat. Nanotechnol.* **8**, 625 (2013).
- [7] P. Soltan-Panahi, J. Struck, P. Hauke, A. Bick, W. Plenkers, G. Meineke, C. Becker, P. Windpassinger, M. Lewenstein, and K. Sengstock, *Nat. Phys.* **7**, 434 (2011).
- [8] L. Tarruell, D. Greif, T. Uehlinger, G. Jotzu, and T. Esslinger, *Nature (London)* **483**, 302 (2012).
- [9] G. De Simoni, A. Singha, M. Gibertini, B. Karmakar, M. Polini, V. Piazza, L. N. Pfeiffer, K. W. West, F. Beltram, and V. Pellegrini, *Appl. Phys. Lett.* **97**, 132113 (2010).
- [10] K. K. Gomes, W. Mar, W. Ko, F. Guinea, and H. C. Manoharan, *Nature (London)* **483**, 306 (2012).
- [11] D. Torrent and J. Sánchez-Dehesa, *Phys. Rev. Lett.* **108**, 174301 (2012).
- [12] O. Peleg, G. Bartal, B. Freedman, O. Manela, M. Segev, and D. N. Christodoulides, *Phys. Rev. Lett.* **98**, 103901 (2007).
- [13] S. Bittner, B. Dietz, M. Miski-Oglu, P. Oria Iriarte, A. Richter, and F. Schäfer, *Phys. Rev. B* **82**, 014301 (2010).
- [14] M. C. Rechtsman, J. M. Zeuner, A. Tünnermann, S. Nolte, M. Segev, and A. Szameit, *Nat. Photonics* **7**, 153 (2012).
- [15] M. C. Rechtsman, J. M. Zeuner, Y. Plotnik, Y. Lumer, D. Podolsky, F. Dreisow, S. Nolte, M. Segev, and A. Szameit, *Nature (London)* **496**, 196 (2013).
- [16] M. Bellec, U. Kuhl, G. Montambaux, and F. Mortessagne, *Phys. Rev. B* **88**, 115437 (2013).
- [17] E. A. Cerda-Méndez, D. N. Krizhanovskii, K. Biermann, R. Hey, M. S. Skolnick, and P. V. Santos, *Phys. Rev. B* **86**, 100301 (2012).
- [18] N. Y. Kim, K. Kusudo, C. Wu, N. Masumoto, A. Löffler, S. Höfling, N. Kumada, L. Worschech, A. Forchel, and Y. Yamamoto, *Nat. Phys.* **7**, 681 (2011).
- [19] N. Y. Kim, K. Kusudo, A. Löffler, S. Höfling, A. Forchel, and Y. Yamamoto, *New J. Phys.* **15**, 035032 (2013).
- [20] K. Kusudo, N. Y. Kim, A. Löffler, S. Höfling, A. Forchel, and Y. Yamamoto, *Phys. Rev. B* **87**, 214503 (2013).
- [21] A. Dousse, J. Suffczyński, A. Beveratos, O. Krebs, A. Lemaître, I. Sagnes, J. Bloch, P. Voisin, and P. Senellart, *Nature (London)* **466**, 217 (2010).
- [22] M. Galbiati, L. Ferrier, D. D. Solnyshkov, D. Tanese, E. Wertz, A. Amo, M. Abbarchi, P. Senellart, I. Sagnes, A. Lemaître, E. Galopin, G. Malpuech, and J. Bloch, *Phys. Rev. Lett.* **108**, 126403 (2012).
- [23] E. L. Shirley, L. J. Terminello, A. Santoni, and F. J. Himpsel, *Phys. Rev. B* **51**, 13614 (1995).
- [24] A. Bostwick, T. Ohta, T. Seyller, K. Horn, and E. Rotenberg, *Nat. Phys.* **3**, 36 (2006).
- [25] E. Wertz, L. Ferrier, D. D. Solnyshkov, P. Senellart, D. Bajoni, A. Miard, A. Lemaître, G. Malpuech, and J. Bloch, *Appl. Phys. Lett.* **95**, 051108 (2009).
- [26] L. Ferrier, E. Wertz, R. Johne, D. D. Solnyshkov, P. Senellart, I. Sagnes, A. Lemaître, G. Malpuech, and J. Bloch, *Phys. Rev. Lett.* **106**, 126401 (2011).
- [27] See Supplemental Material at <http://link.aps.org/supplemental/10.1103/PhysRevLett.112.116402> for further details on the condensation dynamics and a 2D Schrödinger equation simulation.
- [28] F. Manni, K. G. Lagoudakis, R. André, M. Wouters, and B. Deveaud, *Phys. Rev. Lett.* **109**, 150409 (2012).
- [29] C. W. Lai, N. Y. Kim, S. Utsunomiya, G. Roumpos, H. Deng, M. D. Fraser, T. Byrnes, P. Recher, N. Kumada, T. Fujisawa, and Y. Yamamoto, *Nature (London)* **450**, 529 (2007).
- [30] D. Tanese, H. Flayac, D. Solnyshkov, A. Amo, A. Lemaître, E. Galopin, R. Braive, P. Senellart, I. Sagnes, G. Malpuech, and J. Bloch, *Nat. Commun.* **4**, 1749 (2013).
- [31] I. L. Aleiner, B. L. Altshuler, and Y. G. Rubo, *Phys. Rev. B* **85**, 121301 (2012).
- [32] A. Petrescu, A. A. Houck, and K. Le Hur, *Phys. Rev. A* **86**, 053804 (2012).
- [33] S. D. Huber and E. Altman, *Phys. Rev. B* **82**, 184502 (2010).
- [34] C. Wu and S. Das Sarma, *Phys. Rev. B* **77**, 235107 (2008).
- [35] P. E. Allain and J. N. Fuchs, *Eur. Phys. J. B* **83**, 301 (2011).
- [36] T. Ozawa and I. Carusotto, *arXiv:1307.6650*.